ARL

US Army Research Laboratory

Ultrafast Spectroscopic Noninvasive Probe of Vertical Carrier Transport in Heterostructure Devices

by Blair C Connelly, Grace D Metcalfe, and Stefan Svensson

NOTICES

Disclaimers

The findings in this report are not to be construed as an official Department of the Army position unless so designated by other authorized documents.

Citation of manufacturer's or trade names does not constitute an official endorsement or approval of the use thereof.

Destroy this report when it is no longer needed. Do not return it to the originator.

US Army Research Laboratory

Ultrafast Spectroscopic Noninvasive Probe of Vertical Carrier Transport in Heterostructure Devices

by Blair C Connelly, Grace D Metcalfe, and Stefan Svensson
Sensors and Electron Devices Directorate, ARL

REPORT DOCUMENTATION PAGE					*Form Approved* *OMB No. 0704-0188*
Public reporting burden for this collection of information is estimated to average 1 hour per response, including the time for reviewing instructions, searching existing data sources, gathering and maintaining the data needed, and completing and reviewing the collection information. Send comments regarding this burden estimate or any other aspect of this collection of information, including suggestions for reducing the burden, to Department of Defense, Washington Headquarters Services, Directorate for Information Operations and Reports (0704-0188), 1215 Jefferson Davis Highway, Suite 1204, Arlington, VA 22202-4302. Respondents should be aware that notwithstanding any other provision of law, no person shall be subject to any penalty for failing to comply with a collection of information if it does not display a currently valid OMB control number. **PLEASE DO NOT RETURN YOUR FORM TO THE ABOVE ADDRESS.**					
1. REPORT DATE *(DD-MM-YYYY)* March 2016		**2. REPORT TYPE** Director's Research Initiative (DRI)		**3. DATES COVERED (From - To)** October 2012–September 2015	
4. TITLE AND SUBTITLE Ultrafast Spectroscopic Noninvasive Probe of Vertical Carrier Transport in Heterostructure Devices				**5a. CONTRACT NUMBER**	
				5b. GRANT NUMBER	
				5c. PROGRAM ELEMENT NUMBER	
6. AUTHOR(S) Blair C Connelly, Grace D Metcalfe, and Stefan Svensson				**5d. PROJECT NUMBER** FY13-SED-009	
				5e. TASK NUMBER	
				5f. WORK UNIT NUMBER	
7. PERFORMING ORGANIZATION NAME(S) AND ADDRESS(ES) US Army Research Laboratory ATTN: RDRL-SEE-I Aberdeen Proving Ground, MD 21005-5066				**8. PERFORMING ORGANIZATION REPORT NUMBER** ARL-TR-7618	
9. SPONSORING/MONITORING AGENCY NAME(S) AND ADDRESS(ES)				**10. SPONSOR/MONITOR'S ACRONYM(S)**	
				11. SPONSOR/MONITOR'S REPORT NUMBER(S)	
12. DISTRIBUTION/AVAILABILITY STATEMENT Approved for public release; distribution is unlimited.					
13. SUPPLEMENTARY NOTES					
14. ABSTRACT A major issue limiting the performance of many optoelectronic (OE) devices is poor carrier transport in the vertical direction across heterointerfaces. To address this problem, we have developed unique ultrafast spectroscopic techniques to measure directly vertical carrier transport properties in heterostructure devices over a widely tunable spectral range from the visible through long-wavelength infrared. Our approach merges 2 powerful ultrafast spectroscopy techniques, pump-probe spectroscopy and time-domain terahertz (THz) spectroscopy, into a double-pump-probe THz technique. The time-resolved detection of THz radiation induced by a second pump pulse tuned to the absorption edge of a device layer of interest provides information on nonequilibrium transients of the carrier dynamics and internal electric fields as a function of delay after the injection of carriers from an initial pump pulse. For measurements in infrared materials and devices, time-of-flight techniques using pump-probe spectroscopy and optically gated upconversion were developed. These ultrafast spectroscopy techniques are used to study transport in Army-relevant OE heterostructure devices.					
15. SUBJECT TERMS Director's Research Initiative, DRI, vertical transport, ultrafast spectroscopy, pump-probe spectroscopy, terahertz, THz spectroscopy, heterostructure devices, semiconductors					
16. SECURITY CLASSIFICATION OF:			**17. LIMITATION OF ABSTRACT**	**18. NUMBER OF PAGES**	**19a. NAME OF RESPONSIBLE PERSON** Blair C Connelly
a. REPORT Unclassified	**b. ABSTRACT** Unclassified	**c. THIS PAGE** Unclassified	UU	38	**19b. TELEPHONE NUMBER (Include area code)** 301-394-2133

Contents

List of Figures

INTENTIONALLY LEFT BLANK.

1. Objective

A major issue limiting the efficiency of many optoelectronic (OE) devices is poor carrier transport across heterointerfaces. A thorough understanding of the carrier dynamics is necessary to overcome material limitations and improve the performance of the devices. While device performance is often limited by carrier transport in the vertical direction, conventional approaches to measure carrier transport properties typically probe transport in the lateral direction. Vertical transport can vary significantly from lateral transport in heterostructure devices where barriers, tunneling, scattering, strong polarization-induced fields, or carrier localization due to Type I or Type II quantum-well structures can effect transport. To address this problem, this Director's Research Initiative (DRI) project sought to investigate directly the vertical carrier transport properties in Army-relevant semiconductor materials and devices by developing and applying noninvasive nondestructive ultrafast optical spectroscopy techniques operating in a spectral region ranging from the visible to long-wavelength infrared (LWIR).

2. Approach

2.1 Background and Motivation

The performance of numerous OE devices depends heavily on the vertical transport efficiency of injected or photogenerated carriers across multilayer heterostructures. For example, the responsivity of a photodetector depends on the photocurrent, which is influenced by mechanisms such as tunneling across junctions, scattering at heterointerfaces, and internal fields. For light-emitting devices, poor charge transport across multilayer heterostructures strongly decreases the overall efficiency and can lead to efficiency droop at high currents.[1]

Typical measurement techniques to characterize transport properties in semiconductors include magnetotransport measurements of the Hall effect[2] and Quantitative Mobility Spectrum Analysis (QMSA),[2–4] which determine carrier densities and mobilities, and even depth information. Unfortunately, these methods typically examine lateral transport and not transport across heterointerfaces or junctions. Although there have been a few attempts to measure vertical transport, the methods are generally indirect and convoluted. For instance, one method applied to InGaAs/InP superlattice *p-n* junctions used a combination of capacitance versus voltage, alternating current (AC) conductivity, and deep-level transient spectroscopy measurements to determine that transport was limited by localization of holes and rapid electron tunneling.[5] However, direct transport properties were

not determined. Another approach used modeling of current versus voltage data to extract contributions to the current from diffusion, trap-assisted tunneling, and generation-recombination processes.[6] Unfortunately, this method is indirect, must assume several modeling parameters, and only determines the minority carrier diffusion length and mobility. An additional shortcoming of applying each of the aforementioned techniques is the necessity to process specially designed electrical contacts that can further require the addition of heavily doped contact layers to the sample structure.

2.2 Experimental Approach

Our approach is to investigate the vertical carrier transport properties in Army-relevant semiconductor materials and devices by developing and applying ultrafast optical spectroscopy techniques. Optical-based approaches have the advantage of being noninvasive and nondestructive and can usually be performed without modification to the sample. To study vertical transport, a novel femtosecond-resolution double-pump-probe THz spectroscopy technique was developed, which merges 2 powerful ultrafast optical spectroscopy methods, pump-probe spectroscopy and time-domain terahertz (THz) spectroscopy (TDTS). In addition, application of time-resolved photoluminescence (TRPL) studies can be used to study carrier recombination processes in conjunction with our new ultrafast double-pump-probe spectroscopy technique to examine more fully ultrafast carrier phenomena in heterostructured materials and devices under nonequilibrium conditions. A schematic of the combined techniques is illustrated in Figs. 1 and 2. Unlike the traditional pump-probe technique, the optical probe pulse we apply for detection also acts as the optical pump pulse for TDTS. In this way, we can examine not only the transient concentration due to an appropriate pump pulse, but also the time-resolved THz radiation induced by the probe pulse. By analyzing the resulting kinetic profile due to the initial pump pulse, one can obtain critical information about the internal electric fields, radiative and nonradiative recombination rates, carrier drift and diffusion times, field screening, and electron and hole velocities. Monitoring the THz emission due to the probe pulse in conjunction with the pump-probe kinetic profile provides additional information on the nonequilibrium transients of the carrier dynamics and internal electric field as a function of delay after the initial injection of carriers from the first pump pulse. THz radiation strongly interacts with free carriers, especially electrons, in a semiconductor. One can therefore probe vertical as well as horizontal carrier transport in a semiconductor by studying the THz generation mechanisms within the semiconductor. The sign (negative or positive) of the direction of carrier transport can also be determined using the polarity of the time-domain THz waveform.
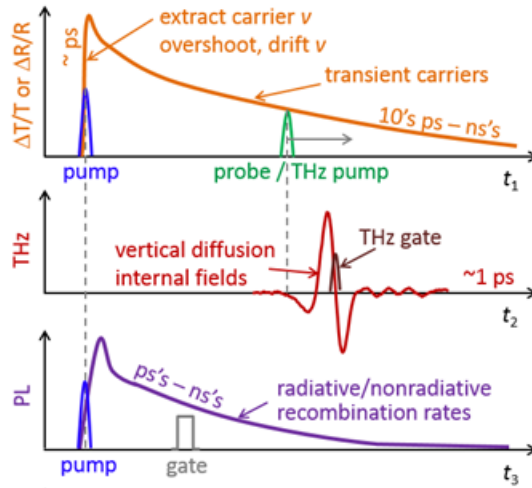
Fig. 1 Schematic of double-pump-probe time-resolved spectroscopy technique
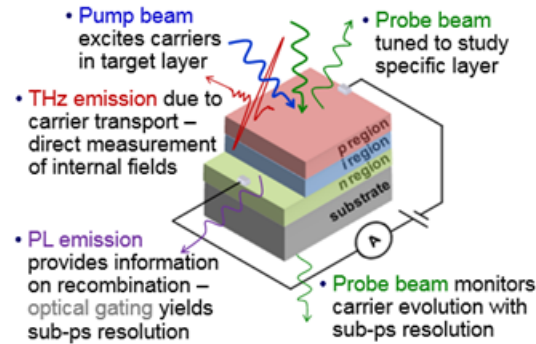
Fig. 2 Illustration of how pump-probe and THz measurements can target specific layers in a heterostructure (i.e., *p-i-n*) device

The double-pump-probe THz technique was previously applied to investigate instantaneous polarization of electron-hole pairs, ballistic transport, electron velocity overshoot, and steady-state drift in GaAs and Si.[7] However, the experiment in Ref. 7 was limited to measurements only at 800 nm and in bulk material. Our approach allows, for the first time, wavelength tunability from the visible through LWIR region and investigation of multilayer heterostructure devices under operating conditions. The wavelength selectivity (~100-fs pulses, tunable between 400 nm and 10 µm) is enabled by leveraging an ultrafast, regeneratively amplified, Ti:Sapphire laser, coupled to an optical parametric amplifier (OPA), difference frequency generator (DFG), and frequency doubler and tripler. Separate pump and probe beams can be specifically tuned to different wavelengths to target distinct layers within a structure.

2.2.1 Double-Pump-Probe THz Spectroscopy System

Figure 3 shows the schematic of the designed and constructed double-pump-probe THz spectroscopy setup. The pump-probe and THz portions of the setup can be operated either separately or in concert. The pump-probe setup operates using a pump beam derived from a regenerative amplifier (operating at 800 nm and 250 kHz) and a probe beam derived from a regenerative-amplifier pumped, tunable OPA capable of producing a beam between 1.2 and 2.4 μm (signal beam, 1.2 to 1.6 μm; idler beam, 1.6 to 2.4 μm). The pump beam can be utilized at 800 nm or frequency doubled to 400 nm. The output of the OPA can be used as is to probe bandgaps in the near-infrared (NIR)/short-wavelength infrared (IR) range, or frequency doubled to the 600-nm to 1.2-μm range, or the signal beam frequency tripled to the 400- to 530-nm range. To achieve this wavelength tunability, a frequency tripler (which can also be used for doubling) was designed, constructed, tested, and found to operate efficiently between 400 and 500 nm. The resulting pump and probe beams are overlapped and focused onto the sample, the pump beam is modulated, and the differential transmission (or reflection) through a sample by the probe is monitored using a lock-in amplifier. While the probe beam is fixed in time, the path of the pump beam traverses an optical delay line, which delays the arrival of the pump beam with respect to the probe beam, and has a scan range of 2 ns with 3-fs resolution. When the optical path lengths (OPLs) are equivalent, $t = 0$ is defined, and times before or after $t = 0$ are achieved by either lengthening or shortening the OPL of the pump beam with the optical delay line. An approximately 150–225-fs temporal resolution is determined by the cross-correlation of the pump and probe beam pulse widths (~100–150 fs each).
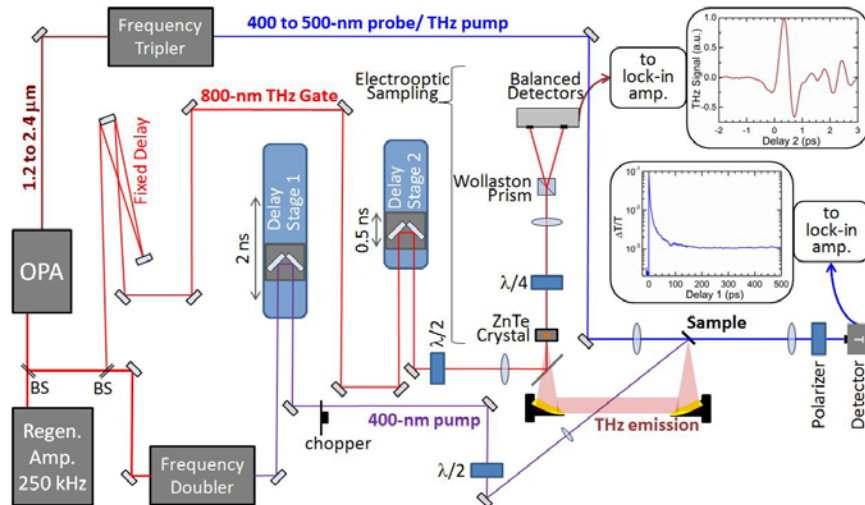

Fig. 3   Double-pump-probe THz spectroscopy system

For the TDTS setup, a pump beam (at 400 or 800 nm) is used to excite free carriers in the sample. Optically generated carriers are accelerated due to diffusion and/or drift, resulting in the emission of THz radiation. The THz emission is collected and focused on a ZnTe crystal by a pair of gold parabolic mirrors. The THz signal is detected using electro-optic sampling using an 800-nm gate pulse incident on the ZnTe crystal, and overlapped with the focused THz signal. For electro-optic sampling, a balanced detector is initially calibrated with no incident THz radiation. The linearly polarized THz-gate beam is transmitted through the ZnTe crystal, and then converted to circularly polarized light with a quarter waveplate. The 2 polarization components of the circularly polarized beam are subsequently split using a Wollaston prism and focused onto a balanced detector that outputs a voltage proportional to the intensity difference of the 2 beams. With no incident THz radiation, the balanced detector outputs zero voltage. Incident THz radiation on the ZnTe crystal causes a polarization rotation of the THz-gate beam, which is measured as a proportional balanced detector output voltage. Temporal resolution of the THz signal is achieved by scanning the optical delay line on either the pump or THz-gate path.

In the integrated setup, the probe beam is fixed in time and the delay of the pump beam is varied. The THz generated by the tunable probe beam, tuned to the band edge of the sample under investigation, is investigated as a function of the delay after the arrival of the initial pump beam. Under most experimental conditions, the THz signal generated by the pump beam is expected to be larger than the probe beam since the photon energy and optical power in the pump beam is typically larger. We therefore employed a clever geometrical approach to minimize detection of THz generation emitted by the pump pulse while maximizing THz generation (and collection) from the probe pulse by using the following facts: THz radiation generated by the photo-Dember effect is zero under normal excitation since the current flow has no component transverse to the emission direction[8]; THz radiation generated is increased at an oblique angle of incidence (maximum at ~75°).[8,9] We employ a near-normal pump excitation with a 45° probe excitation to maximize the signal-to-noise and collection efficiency. To detect the temporal profile of the THz signal, the THz-gate path is varied through small (~1–2 ps) path changes around the OPL of the probe/THz-pump beam as the OPL of the initial pump beam is changed. An initial approach at a fast "real-time" detection of the THz signal involved quickly modulating the pump beam (at 1 kHz), while slowly varying the OPL of the THz-gate path (at 0.5 Hz) using mirrors on a sinusiodally driven speaker and using lock-in detection of the double-modulated signal. The primary oscillations (~1 ps) of the THz signal were successfully detected (see Fig. 4), with a 7.5% error in the timescale linearity at the extremes of the speaker oscillation. Additionally, the slow driving frequency of the speaker used, and necessary

waveform averaging to achieve a satisfactory signal-to-noise ratio led to long acquisition times. It was therefore decided that a variable delay stage would be used in the place of the oscillating speaker.
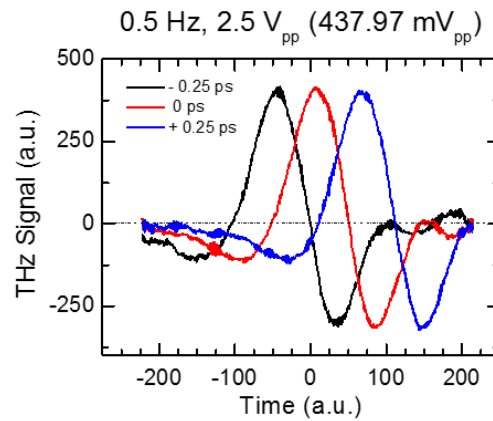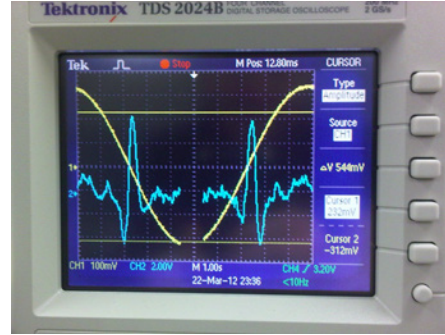
Fig. 4 **"Real-time" THz waveform acquisition (cyan trace). The sinusoidal yellow trace represents the voltage applied to the speaker (top). Linearity investigation of THz waveform acquisition using speaker oscillations (bottom).**

2.2.2 IR Time-of-Flight (ToF) Techniques

To study vertical transport properties in the IR spectral range, we must apply different experimental techniques since detector efficiencies decrease dramatically from the visible toward the IR wavelengths. We explored 2 approaches to detecting the arrival of carriers a known distance from injection, or optical ToF measurements, in IR materials (see sample structure and timing diagram in Fig. 5). In one approach, carriers are optically injected near the sample surface of a mid-wavelength IR (MWIR) InAsSb *nBn* detector structure with a pump beam. Arrival of carriers a known distance from the sample surface are detected using an optical probe of an approximately 2-µm bandgap buffer layer grown on the substrate. In a second approach, photoluminescence (PL) from a "marker" quantum well (QW), with a narrower bandgap than the bulk material, embedded in the absorber layer, a known distance from the surface serves as an indicator of the arrival of injected

6

carriers. By monitoring the PL from the well as a function of time, one can determine the electron transit times and velocities. Temporal resolution of the carrier arrival is achieved using optically gated upconversion of PL from the "marker" well.
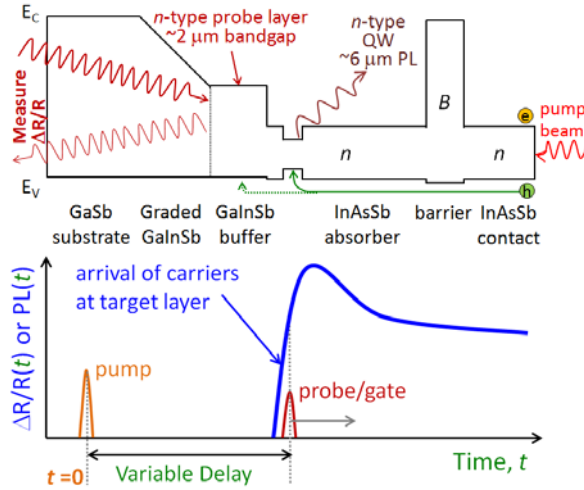
Fig. 5   Sample design for transport measurement in IR materials demonstrating 2 ToF measurement techniques (top). In each approach carriers are injected at the sample surface with a pump beam. Arrival of carriers a known depth into the sample is detected in 2 ways: via differential reflection by a probe beam from the back side of the sample and through optically gated upconversion of PL from an embedded marker well. Timing diagram of ToF transport measurement (bottom). Target layer is either QW or probe layer shown above.

Figure 6 illustrates our design of the optically gated upconversion setup. A regenerative-amplifier pumped OPA is used to generate a 1,250-nm optical-gating beam (signal beam). The 800-nm regenerative-amplifier output is used to excite carriers in the sample (kept at low, <100 K, temperature in a cryostat), rather than the originally planned 2,222-nm idler beam since carriers are generated closer to the surface with the higher-energy 800-nm pulse and will therefore provide better resolution to the arrival of carriers a known depth in the sample. A temporal resolution of less than 250 fs is expected. PL is collected by a pair of gold-coated parabolic mirrors and focused on a nonlinear $AgGaS_2$ crystal used for upconversion of the PL signal. The 1,250-nm gating pulse is delayed with a 2-ns delay stage and incident on the $AgGaS_2$ crystal, which converts 6-µm PL to approximately 1.03 µm through sum frequency generation (SFG). A longer-wavelength gating pulse at 1,250 nm (as compared with 800 nm) was chosen because it provides reasonable phase matching conditions for PL emitted at 6 µm ± 1 µm with only approximately 5° of angle tuning, which will improve the potential of success of the diagnostic technique.
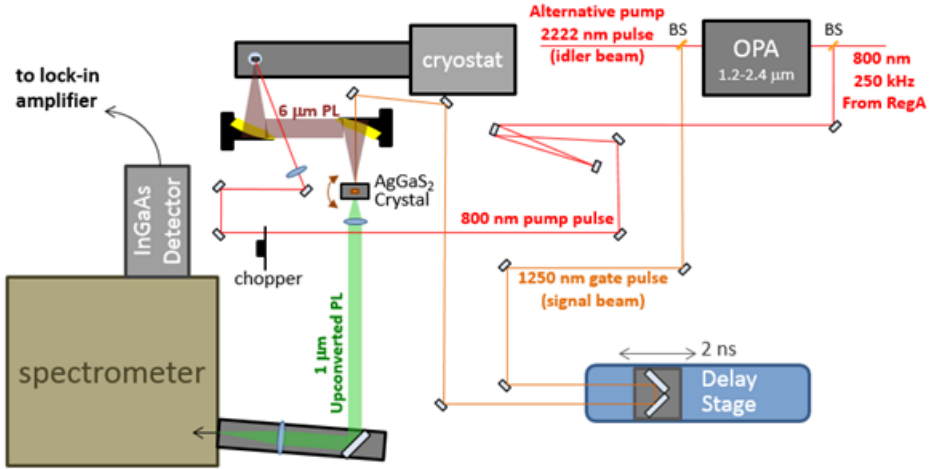
Fig. 6 Experimental setup for optically gated upconversion of MWIR PL

The phase matching conditions are plotted in Fig. 7 for our custom-designed crystal cut at 47.4°; different mixing geometries are investigated, including where both pulses are normally incident (0°) on the crystal or at slightly different angles (~10°). The upconverted PL signal is detected using a lock-in amplifier and a sensitive InGaAs detector through a spectrometer to spectrally filter the incident light. Development of the optically gated IR upconversion PL technique has included the following: measurement of approximately 1-µm PL (the expected SFG wavelength) with the system; characterization of the fast-axis and crystal angle of the nonlinear $AgGaS_2$ crystal by frequency-doubling the 2,222-nm idler beam; alignment of $t = 0$ (where the OPL of the pump and PL collection to the $AgGaS_2$ crystal equals the OPL of the gating pulse) by mixing the 800-nm pump with the 1,250-nm gating pulse resulting in a 488-nm upconverted signal using a beta barium borate (BBO) crystal in the place of the $AgGaS_2$ crystal. For system alignment, we successfully designed, grew, measured, and analyzed samples with a 30-nm-wide "marker" well with approximately 6-µm PL emission embedded in bulk InAsSb material. The upconverted signal was not detected. Current efforts to repeat attempts to observe optically gated, upconverted IR PL use a more sensitive detector (a low-noise InGaAs photomultiplier tube was recently acquired) and redesigned collection optics to improve angular overlap of the PL cone and a narrower gate pulse similar to a Cassegrain telescope design.
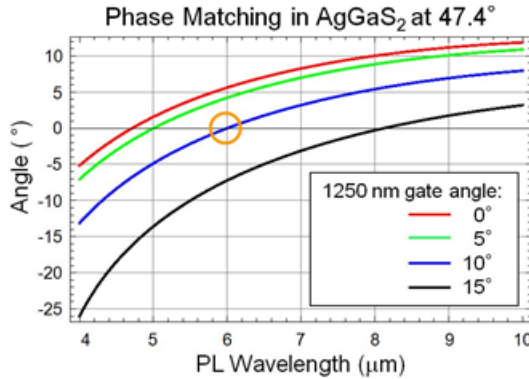
Fig. 7   Phase matching conditions for mixing ~6-µm PL with a 1,250-nm gating pulse at different relative angles of incidence

3.   Results

3.1 Transport Studies in *p-i-n* InGaN/GaN Double Heterostructures

As a preliminary step toward the development of our double-pump-probe THz spectroscopy technique, we applied our optical pump-probe system to evaluate movement of carriers across sample layers through screening of the internal junction and polarization fields. We also applied the TDTS system to determine the direction of electron transport to investigate InGaN/GaN double heterostructure solar cells. A challenge associated with the application of *c*-plane, III-nitride wurtzite heterostructures involves overcoming the strong built-in electric field associated with the termination of large spontaneous and piezoelectric polarizations at heterointerfaces that can significantly affect carrier transport. Conventional *p*-on-*n* (*p*-up) InGaN/GaN double heterostructures solar cells are grown with a layer of *n*-GaN on the substrate, followed by the *i*-InGaN active region, and then finally a *p*-type GaN layer on top. Unfortunately, with this structure design the junction field and polarization field are in opposing directions, which inhibits carrier collection (Fig. 8a). There are different approaches to overcoming the polarization field, including using doping at the GaN/InGaN interfaces to create enough space charge to compensate for the polarization charge at low-In content (Fig. 8b),[10] using a graded heterobarrier,[11] replacing the *p*-GaN layer with *p*-InGaN,[12] or growing samples in the inverted polarity, *n*-on-*p* (*p*-down) configuration (Fig. 8c).[13] To determine the effect of internal electric fields on carrier transport, we performed transport measurements in samples that use the conventional design and in samples that use 2 different approaches to overcome the polarization field: 1) *p*-up samples that use layers of high doping (~5×10^{19} cm^{-3}) at the heterointerfaces to compensate for the polarization charge (obtained through a collaboration with the University of

California, Santa Barbara), and 2) inverted polarity, *p*-down structures that align the polarization field with the junction field (grown at the US Army Research Laboratory [ARL]).
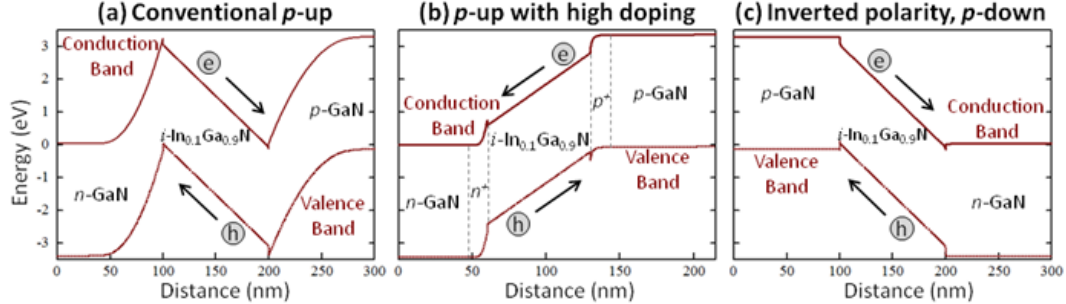
Fig. 8 Calculated band structure of (a) conventional *p*-up, (b) *p*-up with high doping at the interfaces, and (c) inverted polarity, *p*-down InGaN/GaN double heterostructures

Figure 9 plots TDTS measurements using a 400-nm ultrafast laser to excite carriers to an injection level of approximately 10^{17} cm^{-3} in only the *i*-InGaN active region to determine the direction of carrier transport in the samples under investigation. The polarity (sign) of the time-resolved THz pulse is indicative of the direction of electron transport. We use an InAs source for reference (black curve in Fig. 9) since it is well known that THz generated in InAs at low pump fluences is mainly due to electron diffusion away from the surface. We therefore set the phase of the detected THz signal so that a positive polarity corresponds to electron transport away from the sample surface. For the conventional *p*-up sample, we measure a negative THz signal, which is indicative of carrier drift toward the sample surface (*p*-GaN) due to the polarization field dominating transport over the junction field, which is undesirable for device performance. In the *p*-up with high doping and *p*-down samples, we observe electron transport toward the *n*-GaN layer as designed, showing success in overcoming the polarization field.
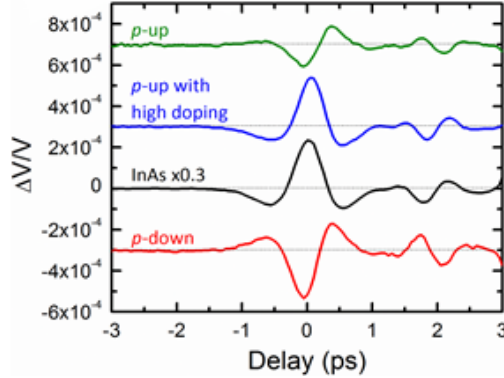
Fig. 9 THz signal from *p*-up, *p*-up with high doping, InAs, and *p*-down InGaN/GaN double heterostructures

3.1.1 Temperature-Dependent Carrier Transport in High-Doping *p*-up Sample

The *p*-up InGaN/GaN double heterostructure with high doping is composed of, from the substrate up, 1 μm of undoped GaN, 2 μm of *n*-GaN ([Si]~2×10^{18} cm^{-3}), 10 nm of n^+-GaN ([Si]~2×10^{19} cm^{-3}), 70 nm of undoped In$_{0.1}$Ga$_{0.9}$N (3-eV bandgap), 40 nm of p^+-GaN ([Mg]~5×10^{19} cm^{-3}), 30 nm of *p*-GaN ([Mg]~2×10^{19} cm^{-3}), with a 15 nm of p^{++}-GaN ([Mg]~$5 \times 10^{19}$ cm^{-3}) cap (the band diagram is plotted in Fig. 8b). Temperature-dependent THz measurements on the *p*-up with high-doping sample are shown in Fig. 10a at 294, 200, 150, 110, 77 and 11 K. The inset to Fig. 10a plots the peak THz signal near $t = 0$ ps as a function of temperature. Efforts to affect the carrier transit time and reverse the field in the active region through electrically forward biasing the diode were unsuccessful, indicating that the doped space charge at the heterointerfaces effectively cancels the polarization field. However, as the temperature is decreased the magnitude of the THz signal decreases, which indicates the acceleration of the carriers is decreasing due to the decrease in the field in the active region.[14] Between 120 and 100 K, the sign of the THz signal is seen to flip, which indicates that the direction of carrier transport has reversed. For temperatures greater than or equal to 120 K, the main THz peak has a positive sign, indicating electron transport is toward the *n*-GaN layer as designed. For temperatures less than or equal to 110 K, the THz signal is inverted, indicating electron transport is toward the *p*-GaN layer and that the polarization field is dominating. We also observe that the amplitude of the THz signal is larger at 294 K (11 K) than at 150 K (77 K) because of a larger electric field.
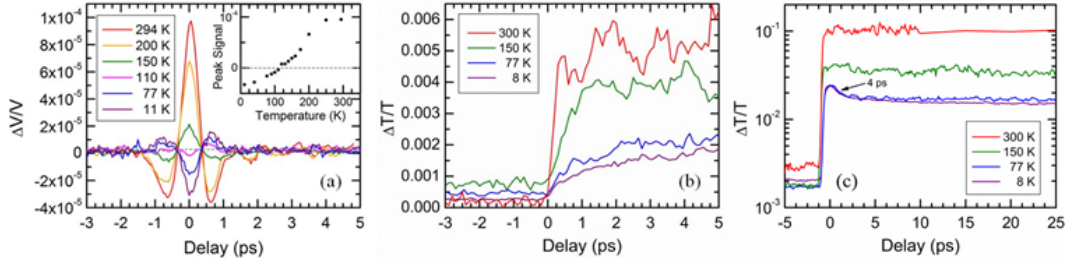
Fig. 10 **(a) THz data as a function of temperature. Peak THz signal as a function of temperature (inset). (b, c) Electroabsorption pump-probe data as a function of temperature in a *p*-up InGaN/GaN double heterostructure with high doping at the heterointerfaces under (b) low injection and (c) high injection.**

To determine carrier transport times, electroabsorption pump-probe measurements were performed as a function of temperature using a 400-nm pump beam to inject carriers into the InGaN layer delayed with respect to a probe beam, which was tuned to the InGaN absorption edge to maximize sensitivity to the differential transmission ΔT. Figure 10 (b and c) plot the change in transmission normalized by the probe transmission $\Delta T/T$, for a sample unperturbed by the pump beam at injection levels of (b) approximately 10^{18} cm^{-3} and (c) approximately 10^{20} cm^{-3} and at 8, 77, 150, and 300 K. Room temperature measurements demonstrate fast, carrier transport toward the *n*-GaN layer. For the low-injection data in Fig. 10b, the system-limited, less than 300-fs rise time at 300 K is indicative of fast removal of excess carriers (likely electrons) from the InGaN layer. As the temperature decreases to 150 K, the electron transit time increases to approximately 1 ps, suggesting that the electric field in the InGaN layer decreases with decreasing temperature. At longer time scales, the $\Delta T/T$ signal relates to electric field screening due to the Franz-Keldysh effect. This field screening signal decreases with decreasing temperature due to fewer carriers leaving the InGaN layer, as the nonlinearity associated with in-well screening is smaller than that due to out-of-well screening.[15] The large difference in $\Delta T/T$ between 150 and 77 K can be attributed to a flipping of the electric field in the InGaN layer as the polarization field begins to dominate between 150 and 77 K and inhibits removal of injected carriers from the InGaN absorption region at low temperature. Modeling and current-voltage measurements show that as the temperature is decreased, it is more difficult for the electrons (holes) to overcome the significant barriers that exist at the InGaN/*n*-GaN(*p*-GaN) interfaces. The measured photocurrent (Fig. 11) and open circuit voltage both decrease as the temperature is decreased, indicating that the internal field is dominating the carrier transport. As the carriers remain at the interfaces of the InGaN region, they cancel the doping-inserted space charge and therefore cause the polarization charge to dominate the internal field and eventually reverse the direction of the field. The electron barrier of approximately 165 meV

and hole barrier of approximately 210 meV are present at all temperatures and hinder device performance, though they only dominate device characteristics at low temperature. The effect of these barriers can be seen further in the high-injection pump-probe data in Fig. 10c, where an approximately 4-ps decay time is observed that can be attributed to an escape time of carriers over the barriers once a sufficient carrier density is reached.
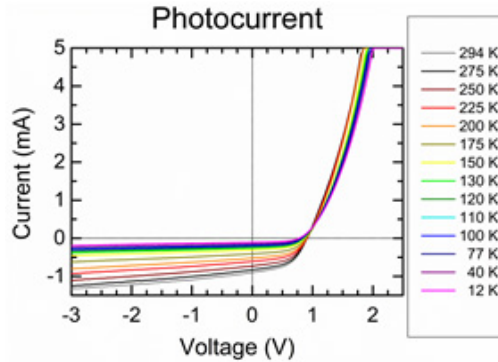
Fig. 11 **Photocurrent as a function of temperature in *p*-up with high-doping InGaN/GaN double heterostructure**

3.1.2 Electroabsorption Measurement of Carrier Velocity in a *p*-down InGaN/GaN Double Heterostructure

For the case of inverted polarity, *p*-down InGaN/GaN double heterostructures, the polarization field is aligned in the same direction as the junction field (as shown in Fig. 8c), and therefore enhances carrier sweep out and capture. Time-resolved electroabsorption pump-probe measurements are used to determine the carrier transit time (average electron and hole velocity in the $In_{1-x}Ga_xN$ region) by monitoring the change in transmission of a sub-bandgap probe beam due to the transport of photogenerated carriers under the built-in internal electric field. Samples with 100-nm-thick $In_{1-x}Ga_xN$ layers demonstrate a sharp rise in the electroabsorption signal at all injection levels that is limited by the approximately 200-fs temporal resolution of the system (see Fig. 12a). Under high injection a fast, approximately 4-ps decay time is observed, which is interpreted as an electron escape time from the InGaN layer due to a barrier at the heterointerface. Both the fast rise time and decay do not show a variation with sample temperature and can therefore be attributed to transport phenomena. Samples with a 200-nm $In_{1-x}Ga_xN$ layer show an increased decay time (>40 ps) and consequently longer escape time in the reduced built-in field under high injection, and an increase in the signal rise time as the carrier density is decreased (see Fig. 12b), which is indicative of time-resolved carrier transport.
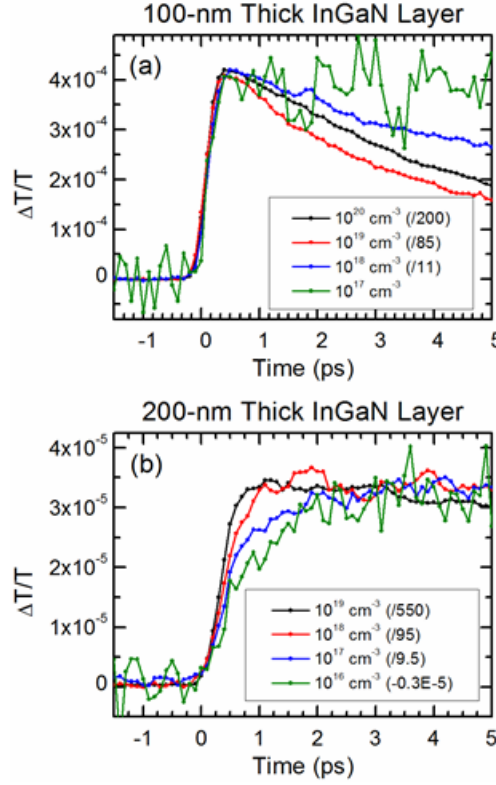
**Fig. 12** **Normalized electroabsorption pump-probe data at several injection levels on n-GaN/i-In$_{1-x}$Ga$_x$N/p-GaN heterostructures with (a) 100-nm-thick In$_{1-x}$Ga$_x$N layer, which demonstrates a fast rise at all injections; (b) 200-nm-thick In$_{1-x}$Ga$_x$N layer where the rise time increases with decreasing pump power, which is indicative of time-resolved carrier transport**

To determine carrier velocities in the 200-nm-thick i-layer (structure: n-GaN/i-In$_{0.093}$Ga$_{0.907}$N/p-GaN), the rise of the low-injection electroabsorption data using a 400-nm pump and 428-nm (6-nm bandwidth) probe beam was fit using Eq. 1:

$$\frac{\Delta T(t)}{\Delta T(\infty)} = \left\{ \left[\int v_e dt - \int v_h dt \exp(-\alpha d) + \alpha^{-1} \left[1 - \exp(-\alpha \int v_h dt) + \exp(-\alpha d)[1 - \exp(\alpha \int v_e dt)] \right] \right] \right\} \Big/ d \left[1 - \exp(-\alpha d) \right], \quad (1)$$

where d is the thickness of the In$_{1-x}$Ga$_x$N layer, α is the absorption coefficient, t is the time delay between the pump and probe beams, and v_e and v_h are the electron and hole velocities, respectively. The change in transmission is normalized by the change in transmission after the carriers have traversed the In$_{1-x}$Ga$_x$N layer, $\Delta T(\infty)$, so that the $\Delta T(t)/\Delta T(\infty)$ bleaching curve reaches a value of unity once the carriers have traversed the In$_{1-x}$Ga$_x$N layer. The sample is pumped from both the p-side and the n-side where v_e and v_h are switched in Eq. 1. The resulting fits and determined carrier velocities are plotted in Fig. 13. Electron and hole velocities in the 200-nm-thick InGaN sample ($3.3 \pm 0.5 \times 10^7$ cm/s and $6.7 \pm 0.3 \times 10^6$ cm/s, respectively, in an internal electric field of ~150 kV/cm) were determined for the first time in any InGaN material from the rise of the electroabsorption signal. The

measured electron velocity was seen to be larger than the saturation velocity in GaN at a similar field,[17] indicating the observation of velocity overshoot.
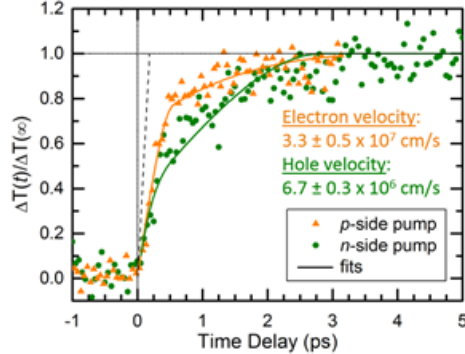
Fig. 13 **Low-injection electroabsorption data on an n-GaN/ i-In$_{1-x}$Ga$_x$N/p-GaN heterostructure with a 200-nm-thick In$_{1-x}$Ga$_x$N layer for the sample being pumped from the n side (front, green circles) and from the p side (back, orange triangles). Fits for carrier velocity are shown as the solid line on each respective curve. The ~190-fs system response is shown as the dotted line.**

3.2 Cross-Well Transport Study

Pump-probe spectroscopy with sub-picosecond resolution is used to study transport across multiple GaN/InGaN interfaces in a c-plane, multiple quantum well (MQW) p-GaN/ i-InGaN/GaN MQW layer/ n-GaN solar cell structure. The InGaN/GaN MQW layer is composed of 50 2.2-nm-thick In$_{0.2}$Ga$_{0.8}$N wells and 4.9-nm-thick GaN barriers. The resulting energy band structure (shown in Fig. 14 for a single well) results in a "saw tooth" potential that inhibits the transport of carriers. Carriers are excited only in the InGaN active region using a 400-nm pump beam, and the differential transmission and reflection are monitored using a probe beam tuned across the band edge as a function of delay with respect to the pump beam and as a function of electrical bias between –10 and +2 V.
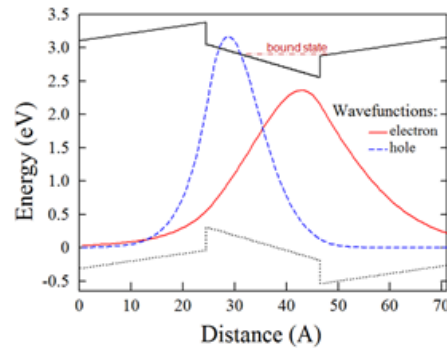
Fig. 14 **Energy band diagram of a single well in MQW p-i-n sample at 0 V bias. Sample structure is composed of 50 wells across a 355-nm-thick i region.**

Data (not shown) taken as a function of wavelength was positive (negative) when probed above (below) the band gap, with the initial rise (fall) due to bleaching from decreased absorption, followed by screening effects as the carriers moved across the sample. It was necessary to create an optically generated carrier density that was significantly high enough to perturb the in-well and global electric fields to produce a notable change in the observed differential reflection signal, $\Delta R/R$. It is important to note that although at these high-injection levels the internal electric fields are appreciably changed by the optical pulse, changing the sample structure, information on the qualitative trends can still be used to try to understand the behavior of optically generated carriers. To improve our understanding in the future, a detailed modeling effort will be necessary to form firm conclusions. Figure 15 plots $\Delta R/R$, at an intermediate injection level, where a variation in the $\Delta R/R$ signal is observed as a function of applied bias. On the longer timescale, the signal is seen to rise then decay with the peak occurring at earlier times as the reverse bias, and consequently internal electric field, is increased. This behavior suggests that the observed trend is related to transport because carriers are more quickly swept through the i region and the field is increased. The –10 V data peaks at 410 ps; the –5 V data peaks at 840 ps; and the time for the 0 and 2 V data is longer than the range of the delay stage. On the shorter timescale, the initial slope, which likely relates to electron transit time, is seen to depend on the bias voltage: the –5, 0, and +2 V times 1.5, 2.9, and 4.7 times longer than –10 V data, respectively. To first order, the peak time can be considered a total transit time hole transport, suggesting that carrier transport across the structure is slow under typical forward bias operating conditions of a solar cell, and that holes may not traverse the entire structure.
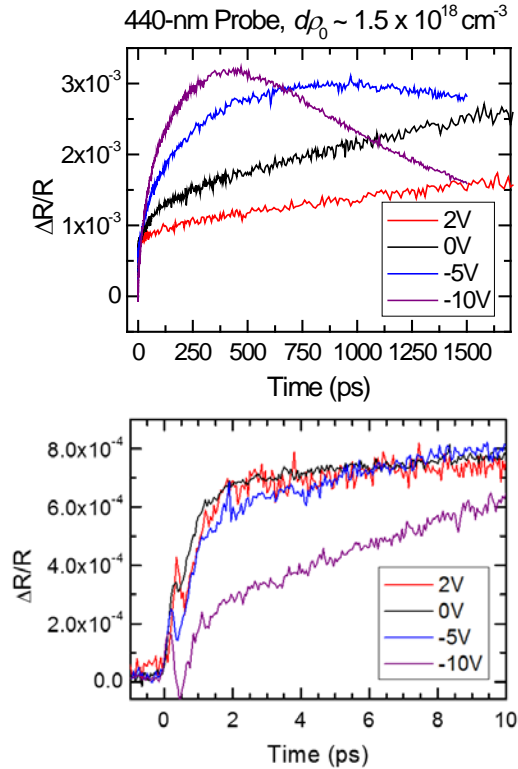
Fig. 15   Differential reflection on MQW InGaN/GaN double heterostructure as a function of electrical bias on 2 timescales

Similar behavior in differential transmission data has been previously observed in InGaAs/GaAs and Ge/SiGe MQW *p-i-n* structures,[18,19] which described the transport as a convolution of 3 screening effects: escape of carriers from the well (g_1), drift of carriers across the depletion layer (electrons, g_{2e}; holes, g_{2h}), and diffusion of the voltage transient across the *p* and *n* electrode (g_3).[20] Attempts to apply the model presented in those works on the MQW InGaN/GaN sample demonstrated that a more detailed study is necessary. Figure 16 plots the ΔR/R data taken at –10 V bias along with the transport model. Livescu et al.[20] suggest a long time constant (~300–400 ps) for the diffusion of the voltage transient for our large (~125–150 µm) pump beam spot, which results in an electron drift time of approximately 10 ps and a hole drift time of approximately 600 ps. This fit does not, however, match the faster rise behavior for 300 ps. The 300-ps behavior is better matched using a shorter, approximately 20-ps diffusion voltage transient time but then requires a much slower hole drift time of approximately 1.4 ns to fit the greater than 500-ps data to go along with the approximately 10-ps electron drift time. If we assume a 10-ps drift time, an average electron velocity of 3.6×10^6 cm/s in a 360-kV net field can be approximated, which is an order of magnitude smaller than the velocity observed in bulk GaN at a similar field. It has, however, been demonstrated that tunneling is the dominant transport mechanism in this structure,[21]

and tunneling is neglected in the model presented here, requiring more analysis. Future work to model the physical phenomena of carrier transport more carefully across a "saw tooth" potential to develop a better understanding of this data and determine expected electron and hole drift times is planned.
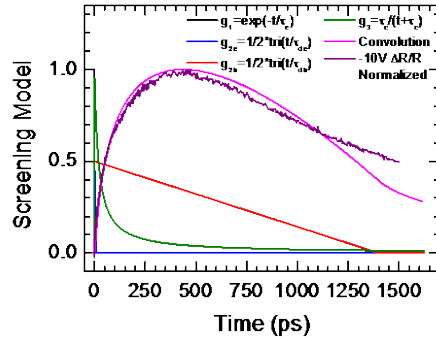

Fig. 16   Transport model applied to ΔR/R data under a –10 V bias

3.3 ToF Measurement in IR Materials

To measure the transit time of optically generated carriers in the structure in Fig. 5 from the surface of the InAsSb absorber/contact layer using a pump-probe technique, it is necessary to measure differential reflection from the GaInSb buffer layer from the backside of the sample because the higher energy probe beam is fully absorbed by the narrow bandgap InAsSb layer(s). This necessitates considerable changes to be made to the sample design. In the previously used GaInSb graded layer (which provided a virtual substrate [VS] with grading of the lattice constant from the GaSb substrate to the GaInSb buffer and InAsSb absorber), significant absorption of the approximately 40-nm bandwidth probe beam occurs in the graded layer, which clouds the desired measurement of differential absorption in the targeted buffer layer. We therefore modified the sample design to use an Al-containing AlInSb grading to widen the bandgap of the graded layer and provide optical access to the buffer layer from the backside of the sample.

Sample growth and design began with unstrained, unrelaxed InAsSb with a targeted absorption wavelength of 7 μm. This followed our standard strategy of using In grading to increase the lattice constant, with a corresponding Al-dominated grade to achieve larger bandgaps, ending with AlInSb, which is also the compound for the VS. To test the feasibility of probing a buffer layer from the backside, the requirement was that the layer should absorb in the 1.6–2.4-μm range. We set the target to 2 μm and considered the options of using a Ga- or Al-based grading strategy for the initial buffer layer. The probe layer could be either AlInSb or GaInSb. The Al-containing version, however, would need to contain approximately 80% In, which would generate a very large lattice constant, and, consequently, a

large number of defects. The Ga version, on the other hand, only required approximately 25% In. We could then use a Ga-grading strategy with a Ga-containing VS as shown in Fig. 17 (top), but decided that the slow bandgap change might make the absorbing properties of the total structure less distinct. Therefore, the final choice was to combine an Al-based grade and a Ga-based VS, which we had not attempted before. This resulted in the bandgap profile shown in Fig. 17 (bottom). Here the entire graded buffer is transparent to the 2 μm absorption of the probe layer. This structure was grown and came out very close to the design targets, with a test structure containing the VS with a 1.5-μm-thick GaInSb probe layer delivered.
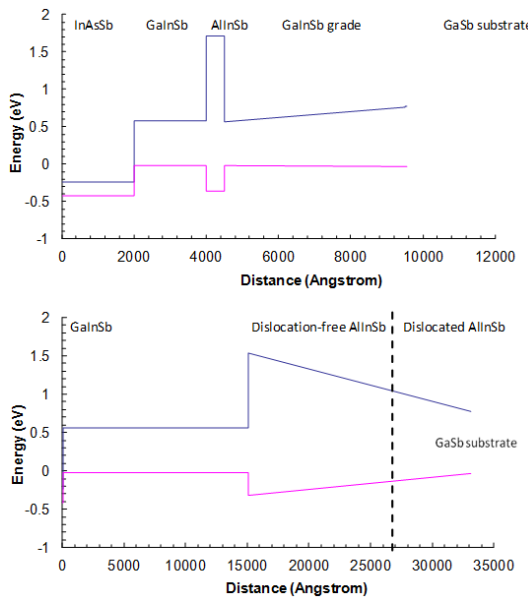
Fig. 17 **Bandgap profiles of a Ga-grade on GaSb with a GaInSb VS for 2-μm absorption (top). A possible AlInSb barrier-layer is also shown as well as an InAsSb layer for LWIR absorption. Bandgap profiles of the selected Al-grade on GaSb with a GaInSb VS for 2-μm absorption (bottom).**

The GaInSb buffer layer was grown 1.5 μm thick to ensure that the probe beam absorption is minimal in the InAsSb layer grown on top, since that layer would absorb any of the probe beam transmitted by the buffer layer and would consequently contribute to the reflected probe and obscure our results (transmission on new VS with buffer layer is shown in Fig. 18). Given a maximum absorption coefficient of 10^4 cm^{-1} (on the short-wavelength side of the absorption edge), we expect a 1.5-μm-thick buffer layer to transmit approximately 22% of the probe beam. Further, if the GaInSb layer were grown too thick, the differential reflection of the probe beam would not be sensitive to carriers arriving at the front-side of the buffer. Using this design, ToF measurements can now be applied to samples grown with an InAsSb layer with greater than a 5 μm thickness. A very thick layer allows

the pump beam to be absorbed close to the surface (and not at all near the bottom of the layer), providing a longer transit distance, and allowing direct probing of the InAsSb layer by tuning the probe beam to an energy below the buffer layer's band edge. When probing the buffer layer, we only expected to see the arrival of holes, since there is a significant barrier to electrons in the conduction band at the GaInSb/InAsSb interface. Probing the InAsSb layer directly is sensitive to the arrival of electrons, enabling measurement of the velocities of both charge carriers.
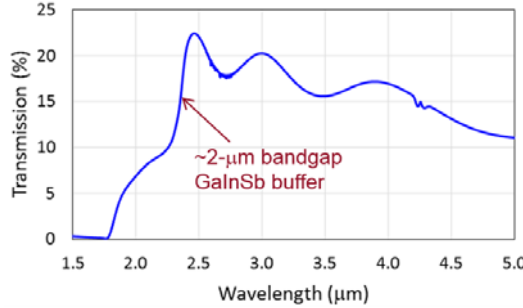
Fig. 18   Transmission measurement in newly designed VS

Figure 19 plots the differential reflection result on the GaInSb buffer layer and demonstrates the realization of our NIR pump-probe system. The rise time of the pump-probe signal is approximately 200 fs, demonstrating the temporal resolution of our system. Future work will include applying this measurement to a *nBn* detector structure or other heterostructure to measure the ToF of injected carriers across an IR absorber layer.
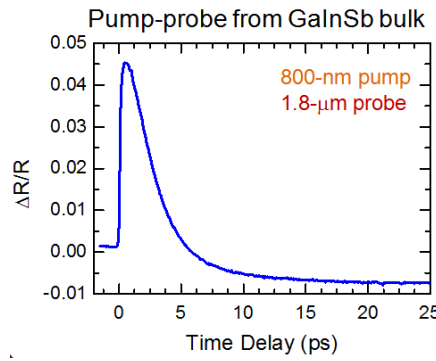
Fig. 19   Differential reflection on NIR GaInSb buffer layer for IR detector structure

3.4 Double-Pump-Probe THz Measurements

To test the double-pump-probe THz spectroscopy technique, initial measurements were made on a bulk *p*-type InAs sample, where the dominant transport mechanism of optically generated carriers is diffusion of electrons and holes away from the sample surface at different velocities (leading to a Dember field), and a GaAs *p-i-n*

homojunction composed of approximately 450-nm total thickness of *p*-type GaAs layers (of varying doping densities), a fully depleted 100-nm-thick *i* layer, and a 2-µm *n*-type base layer. An 800-nm pump beam with an approximately 2-mm spot size is used to inject the initial packet of carriers into the sample, while a second less than 1-mm 800-nm pulse was used to excite the THz at a variable delay with respect to the initial pulse; the power of both beams was approximately 8 mW (though lower powers were tested on the InAs sample with minimal changes to the observed data). Figure 20 plots the peak of the THz waveform at $t = 0$ ps of the THz-gating pulse for electro-optic sampling for both samples. For the InAs sample (Fig. 20 [top]), the detected THz signal generated by the second pulse is seen to increase with a 200- to 400-ps rise time. The increased THz signal is likely due to photo-Dember field generated by the initial pump pulse. For the GaAs *p-i-n* homojunction (Fig. 20 [bottom]), there is an approximately 600-fs decay feature that is not observed in the InAs sample. This is likely due to field screening from carrier drift across the *i* layer of the sample. However, interpretation of the data is difficult because of the long approximately 1-µm absorption length of GaAs distributes carriers across the *p-i-n* structure, and the resulting transport is a combination of drift and diffusion processes. Future work will include measurement in *p-i-n* structures where a majority of carriers are absorbed in the *i* layer and transport can be attributed to drift. Measurements will also be made in other materials, such as the InGaN/GaN MQW sample discussed in Section 3.2 with the pump and probe beams tuned to the band edge.
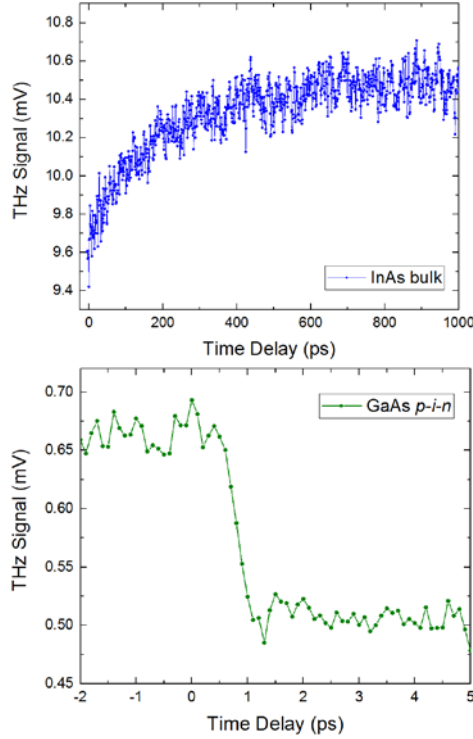
Fig. 20   Double-pump-probe THz signal generated by a THz-pump probe beam as a function of delay after an initial pump pulse in a bulk InAs sample (top) and GaAs *p-i-n* sample (bottom)

4.   Conclusions

The success of this DRI project to investigate directly the vertical carrier transport properties in Army-relevant semiconductor materials and devices was demonstrated through the development and application of new noninvasive nondestructive ultrafast optical spectroscopy techniques. Aspects of carrier transport in InGaN/GaN double heterostructures were illuminated by applying the new pump-probe and THz spectroscopy techniques. A ToF pump-probe measurement for transport measurements in IR materials has been developed and demonstrated, and can be applied to a variety of sample structures. Optically gated upconversion of PL from an embedded marker well has not been successful due to low signal levels and poor detector efficiencies; however, the developed technique can alternatively be used to detect fast features in PL under high injection levels to determine Auger recombination coefficients in bulk IR detector materials where the available signal for detection will be increased, and in NIR and visible materials and devices where the sum frequency generation process in BBO is more robust. Realization of the unique double-pump-probe THz spectroscopy setup was demonstrated on test samples and can now study transport in other heterostructure device structures.

Sustained success will involve continued use of the new ultrafast spectroscopy measurement techniques to support Army programs. The extensive operational wavelength coverage of our developed system allows the examination of materials from the visible through LWIR spectral ranges, such as Type II strained layer superlattices (T2SL) based on III-V technology, which suffer from poor vertical transport due to large thickness layers in the repeated structure, barrier-based device architectures where unknown band offsets influence device performance, and nitride-semiconductor-based OE devices such as LEDs, which suffer from an efficiency droop due to imbalance of charge transport across the junction. Novel device designs to enhance vertical carrier transport and collection will continue to be studied. Information gleaned from these measurements provide ARL and the Army with a deeper understanding of vertical carrier transport in novel heterostructured materials and devices, using the new optical-spectroscopy material-characterization capability for the development and improvement of an extensive range of low-cost high-performance Army-relevant OE devices.

5.   Transitions

The ultrafast spectroscopy techniques developed in this program to measure carrier transport has been transitioned into the III-Nitrides mission program as part of the 2015 6.1 Basic Refresh effort under the project, *Fundamental Studies of Carrier Transport and Vertical Light Emission in Near-UV Heterostructures*. In this program, the capabilities developed during this DRI will be expanded into the near-ultraviolet (UV) region of the spectrum to study the fundamental aspects of transport across heterostructures in conjunction with internal ARL growth efforts and new advanced modeling efforts to progress our understanding. Future transitions will expand into the development of other materials of importance for applications across the UV, visible, and IR spectral ranges to enhance the understanding of materials and carrier transport, which is needed for improved materials and devices.

Publications and Significant Presentations to Date

- Connelly BC, Sampath AV, Enck RW, Gallinat CS, Kelly SB, Woodward NT, Metcalfe GD, Baker DR, Lundgren CA, Shen H, Reed ML, et al. Polarization enhanced transport of hot carriers in liquid/InGaN semiconductor junctions. 20th International Conference on Solid State Ionics; 2015 June 15; Keystone (CO).

- Connelly BC, Metcalfe GD, Svensson S. Ultrafast spectroscopic noninvasive probe of vertical carrier transport in heterostructure devices. TAB Review. 2015 June 10–12; Adelphi (MD).

- Connelly BC, Gallinat CS, Woodward NT, Enck RW, Metcalfe GD, Tompkins R, Jones KA, Shen H, Wraback M. Time-resolved electroabsorption measurement of carrier velocity in inverted polarity $In_{1-x}Ga_xN$/GaN Heterostructures due to internal electric fields. International Conference on the Physics of Semiconductors (ICPS); 2014 Aug 10–15; Austin (TX).

- Woodward NT, Enck RW, Gallinat CS, Young EC, Speck JS, Shen H, Wraback M. The origin of lateral electric fields in *c*-plane III-V nitrides. International Conference on the Physics of Semiconductors (ICPS); 2014 Aug 10–15; Austin (TX).

- Connelly BC, Gallinat CS, Woodward, NT, Enck RW, Metcalfe GD, Tompkins R, Jones KA, Shen H, Wraback M. Time-resolved electroabsorption measurement of carrier velocity in inverted polarity $In_{1-x}Ga_xN$/GaN heterostructures due to internal electric fields. Physica Status Solidi. C. 2014;11(3-4):682–685.

- Woodward NT, Enck RW, Gallinat CS, Rodak LE, Metcalfe GD, Speck JS, Shen H, Wraback M. Anomalous terahertz emission in *c*-plane InN due to in-plane transport. Physica Status Solid C. 2014;11(3-4):686–689.

- Connelly BC Gallinat CS, Woodward, NT, Enck RW, Metcalfe GD, Tompkins R, Jones KA, Shen H, Wraback M. Time-resolved electroabsorption measurement of carrier velocity in inverted polarity $In_{1-x}Ga_xN$/GaN heterostructures due to internal electric fields. International Conference on Nitride Semiconductors (ICNS), B12.01. 2013; Washington, (DC).

- Woodward NT, Gallinat CS, Metcalfe GD, Shen H, Wraback M, Speck JS. Anomalous terahertz emission in *c*-plane InN due to in-plane transport. International Conference on Nitride Semiconductors (ICNS); B12.05. 2013; Washington (DC).

- Connelly BC, Woodward NT, Metcalfe GD, Rodak N, Das C, Reed M, Sampath AV, Shen H, Wraback M, Farrell RM, et al. Temperature-dependent carrier transport in a *p*-GaN/*i*-InGaN/*n*-GaN solar cell heterostructure using ultrafast spectroscopy. Conference on Lasers and Electro Optics (CLEO); CTh1M.7. 2013 June 9–14; San Jose (CA).

- Woodward NT, Gallinat CS, Enck RW, Metcalfe GD, Shen H, Wraback M. Polarization and interface effects on THz emission from c-plane InGaN/GaN heterostructures. March meeting of APS; Y23.00010. 2013; Baltimore (MD).

- Connelly BC, Gallinat CS, Woodward, NT, Enck RW, Metcalfe GD, Tompkins R, Jones KA, Shen H, Wraback M. Time-resolved electroabsorption measurement of electron velocity in InGaN heterostructures due to internal electric fields. March Meeting of APS; T23.00010. 2013; Baltimore (MD).

6.   References

1.   David A, Grundmann MJ. Droop in InGaN light-emitting diodes: a differential carrier lifetime analysis. Applied Physics Letters. 2010;96(10):103504.

2.   Meyer JR, Hoffman CA, Bartoli FJ, Arnold DA, Sivananthan S, Faurie JP. Methods for magnetotransport characterization of IR detector materials. Semiconductor Science and Technology. 1993;8:805–823.

3.   Swartz CH, Tompkins RP, Giles NC, Myers TH, Lu H, Schaff WJ, Eastman LF. Investigation of multiple carrier effects in InN epilayers using variable magnetic field Hall measurements. Journal of Crystal Growth. 2004;269(1):29–34.

4.   Vurgaftman I, Meyer JR, Hoffman CA, Redfern D, Antoszewski J, Faraone L, Lindemuth JR. Improved quantitative mobility spectrum analysis for Hall characterization. Journal of Applied Physics. 1998;84(9):4966.

5.   Lang DV, Sergent AM, Panish MB, Temkin H. Direct observation of effective mass filtering in InGaAs/InP superlattices. Applied Physics Letters. 1986;49(13):812.

6.   Williams GM, DeWames RE. Numerical-simulation of HgCdTe detector characteristics. Journal of Electronic Materials. 1995;24(9):1239–1248.

7.   Hu BB, de Souza EA, Knox WH, Cunningham JE, Nuss MC. Identifying the distinct phases of carrier transport in semiconductors with 10 fs resolution. Physical Review Letters. 1995;74(9):1689–1692.

8.   Shan J, Heinz TF. Terahertz radiation from semiconductors. Ultrafast Dynamical Processes in Semiconductors. 2004;92:1–56.

9.   Zhang X-C, Hu BB, Darrow JT, Auston DH. Generation of femtosecond electromagnet pulses from semiconductor surfaces. Applied Physics Letters. 1990;56(11):1011–1013.

10.   Neufeld CJ, Cruz SC, Farrell RM, Iza M, Lang JR, Keller S, Nakamura S, DenBaars SP, Speck JS, Mishra UK. Effect of doping and polarization on carrier collection in InGaN quantum well solar cells. Applied Physics Letters. 2011;98(24):243507.

11. Chang J-Y, Liou B-T, Lin H-W, Shih Y-H, Chang S-H, Kuo Y-K. Numerical investigation on the enhanced carrier collection efficiency of Ga-face GaN/InGaN p-i-n solar cells with polarization compensation interlayers. Optics Letters. 2011:36(17).

12. Wierer JJ, Fischer AJ, Koleske DD. The impact of piezoelectric polarization and nonradiative recombination on the performance of (0001) face GaN/InGaN photovoltaic devices. Applied Physics Letters. 2010:96(5):051107.

13. Reed ML, Readinger ED, Shen H, Wraback M. n-InGaN∕p-GaN single heterostructure light emitting diode with p-side down. Applied Physics Letters. 2008:93(13):133505.

14. Connelly BC, Woodward NT, Metcalfe GD, Rodak N, Das C, Reed M, Sampath AV, Shen H, Wraback M, Farrell RM, et al. Temperature-dependent carrier transport in a p-GaN/i-InGaN/n-GaN solar cell heterostructure using ultrafast spectroscopy. Conference on Lasers and Electro Optics (CLEO); CTh1M.7. 2013 June 9–14; San Jose (CA).

15. Huang XR, Harken DR, Cartwright AN, Smirl AL, Sánchez-Rojas JL, Sacedón A, Calleja E, Muñoz E. In-well screening nonlinearities in piezoelectric multiple quantum wells. Applied Physics Letters. 1995;67(7):950.

16. Connelly BC, Gallinat CS, Woodward NT, Enck RW, Metcalfe GD, Tompkins R, Jones KA, Shen H, Wraback M. Time-resolved electroabsorption measurement of carrier velocity in inverted polarity In$_{1-x}$Ga$_x$N/GaN heterostructures due to internal electric fields. Physica Status Solidi C. 2014;11(3–4):682–685.

17. Wraback M, Shen H, Carrano JC, Collins CJ, Campbell JC, Dupuis RD, Schurman MJ, Ferguson IT. Time-resolved electroabsorption measurement of the transient electron velocity overshoot in GaN. Applied Physics Letters. 2001;79(9):1303.

18. Claussen SA, Tasyurek E, Roth JE, Miller DAB. Measurement and modeling of ultrafast carrier dynamics and transport in germanium/silicon-germanium quantum wells. Optics Express. 2010;18(25):25596–25607.

19. Wang HS, Effenberger FJ, LiKamWa P, Miller DAB. Ultrafast cross-well carrier transport in a strained multiple-quantum-well InGaAs-GaAs p-i-n modulator. IEEE Journal of Quantum Electronics. 1997;33(2):192–197.

20. Livescu G, Miller DAB, Sizer T, Burrows DJ, Cunningham JE, Gossard AC. High-speed absorption recovery in quantum well diodes by diffusive electrical conduction. Applied Physics Letters. 1989;54(8):748–750.

21. Lang JR, Young NG, Farrell RM, Wu Y-R, Speck JS. Carrier escape mechanism dependence on barrier thickness and temperature in InGaN quantum well solar cells. Applied Physics Letters. 2012;101:181105.

List of Symbols, Abbreviations, and Acronyms

AC	alternating current
ARL	US Army Research Laboratory
BBO	beta barium borate
DFG	difference frequency generator
DRI	Director's Research Initiative
IR	infrared
LWIR	long-wavelength infrared
MQW	multiple quantum well
MWIR	mid-wavelength IR
NIR	near infrared
OE	optoelectronic
OPA	optical parametric amplifier
OPL	optical path length
PL	photoluminescence
PMT	photomultiplier tube
QMSA	Quantitative Mobility Spectrum Analysis
QW	quantum well
SFG	sum frequency generation
TDTS	time-domain terahertz (THz) spectroscopy
THz	terahertz
ToF	time-of-flight
TRPL	time-resolved photoluminescence
UV	ultraviolet
VIS	visible
VS	virtual substrate